Atmos. Chem. Phys., 26, 15291–15307, 2026
https://doi.org/10.5194/acp-26-15291-2026
© Author(s) 2026. This work is distributed under
the Creative Commons Attribution 4.0 License.

Atmospheric Chemistry and Physics
Open Access
EGU

Meteorological normalization of surface ozone variability across warm and cold seasons in China during 2015–2024

Zhenying Ye[1], Run Liu[1], Tingting Hu[2,3], Guoxin Chen[1], and Min Wu[1]

[1]College of Environment and Climate, Institute for Environmental and Climate Research, Jinan University, Guangzhou, 511443, China
[2]Fujian Academy of Environmental Sciences, Fuzhou, 350013, China
[3]Fujian Key Laboratory of Environmental Engineering, Fuzhou, 350013, China

Correspondence: Run Liu (liurun@jnu.edu.cn)

Received: 18 May 2026 – Discussion started: 23 June 2026
Revised: 10 October 2026 – Accepted: 12 October 2026 – Published: 29 October 2026

Abstract. Surface ozone (O_3) concentrations in China have continued to increase, but the roles of meteorological variability and longer-term changes remain uncertain, particularly across seasons and regions. Here, we combined LightGBM-based meteorological normalization with SHapley Additive exPlanations (SHAP) to investigate warm- and cold-season variations in maximum daily 8 h average O_3 (MDA8 O_3) across China during 2015–2024. The models reproduced daily MDA8 O_3 variability reasonably well, with mean testing R^2 values of 0.62 and 0.68 in the warm and cold seasons, respectively. Observed national mean MDA8 O_3 increased by 2.0 and 2.2 $\mu g\,m^{-3}\,yr^{-1}$ in the two seasons, respectively. After meteorological normalization, the corresponding trends were 1.1 and 1.2 $\mu g\,m^{-3}\,yr^{-1}$, indicating that meteorological variability alone cannot fully explain the observed increases. The normalized long-term component may reflect changes in precursor emissions, background O_3, regional transport, and other processes not explicitly represented in the model. SHAP analysis revealed distinct seasonal and regional meteorological associations. During the warm season, temperature and solar radiation were more important in northern inland and basin regions, whereas relative humidity and wind were more important in southern coastal regions. During the cold season, solar radiation dominated across most regions, while relative humidity was more important in the Pearl River Delta. Meteorological contributions generally shifted from negative during 2015–2019 to positive after 2019, amplifying O_3 pollution in several regions. These findings highlight the importance of accounting for seasonal meteorological variability when evaluating long-term O_3 trends in China.

1 Introduction

Surface ozone (O_3) has become an increasingly important air pollutant in many regions of the world, with adverse effects on human health, vegetation, and crop production (Feng et al., 2015; Gong et al., 2021; Chen et al., 2023; He et al., 2023). In China, substantial reductions in primary air pollutants, including SO_2 and $PM_{2.5}$, have been achieved since the implementation of the Air Pollution Prevention and Control Action Plan in 2013. However, surface O_3 concentrations have continued to increase in many regions, limiting further improvements in air quality (Wang et al., 2017; Li et al., 2020; Wang et al., 2022a). This problem is particularly evident in densely populated and highly industrialized regions, such as the North China Plain (NCP), Yangtze River Delta (YRD), Pearl River Delta (PRD), Sichuan-Chongqing Basin (SCB), and Fenwei Plain (FWP), where O_3 pollution exhibits pronounced regional characteristics and complex temporal variability (Lu et al., 2019; Wang et al., 2022b; Ren et al., 2023; Cao et al., 2024b).

The formation and variability of tropospheric O_3 are controlled by coupled effects of precursor emissions, atmo-

spheric chemistry, and meteorological conditions (Li et al., 2016; Wang et al., 2017). Photochemical O_3 production depends nonlinearly on nitrogen oxides (NO_x) and volatile organic compounds (VOCs), resulting in different O_3 sensitivity regimes across regions and seasons (Ren et al., 2022; Wang, 2022a). Meteorological conditions further regulate O_3 formation, accumulation, transport, and removal. High temperature, strong solar radiation, low relative humidity, weak ventilation, and stagnant conditions generally favor photochemical production and near-surface accumulation of O_3, especially during the warm season (Liu et al., 2019; Wang et al., 2025a; Yang et al., 2024). In addition, boundary-layer dynamics and regional transport can modify the vertical mixing and horizontal redistribution of O_3 and its precursors (Li et al., 2016; Wang et al., 2017; Weng et al., 2022; Chen et al., 2025). These processes indicate that observed O_3 variability reflects both changes in precursor emissions and meteorological modulation, and that their relative importance may differ substantially between seasons and regions.

Quantifying the respective roles of meteorological variability and non-meteorological changes is essential for interpreting long-term O_3 trends and evaluating the effectiveness of air-quality management. Several approaches have been used for this purpose, including chemical transport models (CTMs), statistical decomposition methods, and machine-learning-based meteorological normalization (Yang and Zhao, 2023; Li et al., 2022; Guo et al., 2022; Liu et al., 2019; Zhou et al., 2022; Xue et al., 2023; Zhang et al., 2024). CTMs can explicitly represent emissions, chemistry, transport, and deposition processes, and are therefore powerful tools for process-level attribution. However, their results can be sensitive to emission inventories, chemical mechanisms, boundary conditions, and meteorological inputs, which introduces uncertainty in long-term and large-scale applications (Yang and Zhao, 2023; Li et al., 2022). Statistical methods, such as Kolmogorov–Zurbenko filtering and multiple linear regression, provide useful empirical estimates of meteorological and non-meteorological contributions, but they may have limited ability to represent nonlinear chemical responses and interactions among meteorological variables (Liu et al., 2023a). Machine learning provides an alternative framework for capturing nonlinear relationships between O_3 and meteorological predictors and has been increasingly used to remove meteorological variability from air-pollution time series (Grange and Carslaw, 2019; Vu et al., 2019; Grange et al., 2018; Ding et al., 2023; Dai et al., 2023).

Among machine-learning approaches, tree-based ensemble models have been widely applied in air-quality studies because of their ability to handle nonlinear responses, variable interactions, and large observational datasets. LightGBM is a computationally efficient gradient-boosting framework that can provide robust predictive performance for large-scale environmental data (Ke et al., 2017). Recent environmental applications include an interpretable LightGBM–SHAP framework for seasonal analysis of urban heat-island and $PM_{2.5}$ pollution management (Liu and Hang, 2026), as well as LightGBM-based bias correction of O_3 projections from a chemistry–climate model (Ni et al., 2026). When combined with meteorological normalization, such models can estimate the O_3 concentrations expected under average meteorological conditions and thereby separate meteorologically driven variability from longer-term non-meteorological changes (Grange et al., 2018; Vu et al., 2019; Dai et al., 2023). In addition, SHapley Additive exPlanations (SHAP) can be used to interpret trained machine-learning models by attributing model predictions to individual input variables (Lundberg and Lee, 2017; Lundberg et al., 2020). Recent studies have applied interpretable machine-learning approaches to investigate O_3 pollution and its associated factors (Weng et al., 2022; Zhang et al., 2024; Tan et al., 2024; Lyu et al., 2025). However, SHAP values explain how the fitted model attributes its predictions to the input variables. These attributions reflect patterns learned by the model; they do not, by themselves, establish physical causality or quantify the direct physical effect of individual variables on O_3.

Despite these advances, several gaps remain in understanding recent O_3 changes in China. First, many previous studies have focused on individual cities, selected polluted regions, or warm-season O_3 episodes, whereas a consistent national-scale assessment over the most recent decade remains limited (Li et al., 2020; Wang et al., 2022a; Wu et al., 2022; Ding et al., 2023). Second, warm-season O_3 has received much attention because of strong photochemical production and frequent exceedances, but cold-season O_3 changes are also important. Future projections further suggest that O_3 pollution may extend into the non-warm season as declining NO_x emissions weaken the titration effect (Yang et al., 2025a; Wang Y., Wang Y., et al., 2025). During the cold season, weaker photochemistry, reduced NO titration, changes in background O_3, boundary-layer processes, and regional transport may all affect surface O_3 levels (Li et al., 2021; Tong et al., 2023; Wang et al., 2022b). A direct comparison between warm and cold seasons is therefore needed to clarify whether the drivers of O_3 changes differ between high-photochemical and low-photochemical environments. Third, the spatial heterogeneity of meteorological modulation across major polluted regions remains insufficiently quantified, particularly under the recent changes in both emissions and climate variability (Liu and Wang, 2020; Weng et al., 2022; Wang et al., 2025b).

Here, we investigate the interannual variability of MDA8 O_3 across China during the warm and cold seasons from 2015 to 2024. We first characterize the spatial distribution and temporal trends of observed MDA8 O_3 at the national scale and across major polluted regions. We then develop a LightGBM-based meteorological normalization framework to estimate meteorologically normalized O_3 concentrations and to quantify the relative contributions of meteorological variability and meteorologically normalized components to interannual O_3 changes. The meteorologically

normalized component is interpreted as a composite signal that is likely influenced by changes in precursor emissions, background O_3, regional transport, and other slowly varying processes. Finally, we apply SHAP analysis to identify the meteorological variables most strongly associated with O_3 variability across regions and seasons. By comparing warm- and cold-season O_3 changes, this study aims to provide a seasonally resolved understanding of the meteorological modulation and long-term evolution of surface O_3 pollution in China.

2 Data and methods

2.1 Data

This study used hourly surface O_3 observations from the China National Environmental Monitoring Centre (CNEMC) for the period 2015–2024. MDA8 O_3 was used as the primary metric because it is widely applied in studies of surface O_3 pollution and is closely related to air-quality assessment. Quality control excluded monitoring sites with more than 10 % missing hourly records during the study period, including sites whose prolonged consecutive gaps caused the missing-record fraction to exceed this threshold. A total of 1142 monitoring sites were retained for the analysis. The numerical features were standardized before KNN reconstruction. Hourly O_3 reconstruction was limited to short gaps (short_gap ≤ 24 h; hour_window $= \pm 2$ h; doy_window $= \pm 45$ d; features = CO, $PM_{2.5}$, NO_2, SO_2, hour, day_of_year, day_of_week; metric = "euclidean"; min_donors ≥ 20; n_neighbors = 10; weighting = inverse distance) (Saeipourdizaj et al., 2021; Belachsen and Broday, 2022). Only gaps of ≤ 24 h were reconstructed; longer gaps or gaps without sufficient donor support remained missing. Across the 1142 retained sites, KNN-reconstructed values accounted for 4.58 % of all expected hourly O_3 records during 2015–2024. For each station, MDA8 O_3 was defined as the maximum 8 h rolling mean with window end times between 08:00 and 24:00 LT (local time, UTC+8). Each window required at least six valid hourly observations, and a value was retained only when at least 14 valid 8 h rolling-mean windows were available within this period.

Previous studies of O_3 pollution in China have focused mainly on the warm season, but recent evidence indicates that O_3 increases are not confined to photochemically active months and can also extend into the cold season. To examine the seasonal contrast in O_3 variability, we defined May–October as the warm season and November–April as the cold season. For the cross-year cold season, November and December were assigned to the following cold-season year together with January–April. For example, the 2016 cold season refers to November–December 2015 and January–April 2016. This definition separates the high-photochemical and low-photochemical periods and is consistent with previous studies of seasonal O_3 variability in China (Wang et al., 2022a).

Because the first cold season (2015) includes November–December 2014, some stations lack observations for these boundary months. At sites without matched 2014 historical files, we used nearest-neighbor interpolation to obtain daily MDA8 O_3 estimates from the 1 km ChinaHighO_3 Version 3 dataset at each monitoring-site location, filling only missing boundary-period values where valid estimates were available and retaining observed station values (Wei et al., 2022; Yang et al., 2025b). The dataset had a cross-validation R^2 of 0.89 and an RMSE of 15.77 $\mu g\,m^{-3}$ (ChinaHighO_3 Version 3 dataset: https://doi.org/10.5281/zenodo.21811088). Because dataset estimates may differ from station observations at individual sites, we assessed the sensitivity of the national cold-season trend by comparing this treatment with two alternatives: leaving missing values unfilled and excluding November–December 2014. The national cold-season trend retained the same direction and statistical significance under all three treatments. The three scenarios are summarized in Table S1 in the Supplement, and their effects on the national cold-season trend are shown in Fig. S1 in the Supplement, with further details provided in Sect. S1 in the Supplement.

To examine regional differences, we grouped representative cities into five major polluted regions: NCP, YRD, PRD, FWP, and SCB. The regional classification follows previous work on surface O_3 pollution and source-meteorology influences in China (Lu et al., 2019). The detailed city lists for each region are provided in Table S2. Meteorological fields were obtained from the ERA5 reanalysis produced by the European Centre for Medium-Range Weather Forecasts (ECMWF), with a horizontal resolution of $0.25° \times 0.25°$ and an hourly temporal resolution. We selected meteorological variables that are closely related to O_3 photochemical production, atmospheric transport, dilution, and boundary-layer processes. These variables include 2 m temperature (T2M), surface solar radiation downwards (SSRD), total cloud cover (TCC), boundary-layer height (BLH), 10 m zonal and meridional wind components (U10 and V10), surface pressure (SP), relative humidity (RH), and total precipitation (TP). The daily aggregation of meteorological variables followed the approach of Weng et al. (2022), with different averaging periods selected to represent the meteorological conditions most relevant to daytime O_3 formation and transport (Table S3). ERA5 meteorological variables were interpolated to each monitoring site using nearest-neighbor interpolation.

The daily city means of MDA8 O_3 were calculated as arithmetic means of valid station observations, and national and regional daily means as arithmetic means of valid city means across all cities or those listed in Table S2, respectively. The warm- and cold-season annual means were calculated from the corresponding daily means; trends over 2015–2024 were estimated at the site, national, and regional scales using Theil–Sen slopes, with significance assessed using the Mann–Kendall test.

2.2 LightGBM-based meteorological normalization method

In this study, we developed a LightGBM-based prediction model to estimate daily MDA8 O_3 concentrations. LightGBM is a gradient-boosting decision-tree algorithm that is well suited for large environmental datasets because it can capture nonlinear relationships and interactions among predictors while maintaining high computational efficiency (Ke et al., 2017). The target variable was daily MDA8 O_3, and the input predictors included both temporal and meteorological variables. Temporal variables included Unix time, day of year (DOY), and day of week (DOW), which were used to represent long-term changes and recurring seasonal or weekly patterns that are not explicitly explained by meteorological variability. Meteorological predictors included T2M, SSRD, TCC, BLH, U10, V10, SP, RH, and TP, representing thermal, radiative, dynamic, moisture, and boundary-layer conditions relevant to O_3 formation and dispersion. To assess the representation of long-term variation, we compared normalized trends with and without Unix time (Fig. S2 and Sect. S2). Its removal markedly weakened the trends, but Unix time cannot be interpreted as a uniquely non-meteorological signal.

An independent LightGBM model was fitted for each monitoring site and season. Data from 2015–2021 were used for training. Hyperparameters were selected separately for each site and season using time-ordered validation within this period: models were trained on earlier years and evaluated on later years, and the combination with the lowest mean RMSE was retained. Data from 2022 were used for validation, and observations assigned to the 2023–2024 seasonal test period were held out for testing. Model performance was assessed using the coefficient of determination (R^2), root mean square error (RMSE), and mean absolute error (MAE). To assess the sensitivity of the normalized regional patterns to the learning algorithm, we repeated the analysis using a Random Forest (RF) model. The two analyses used the same station data, seasonal definitions, temporal partition, predictors, and normalization procedure; only the learning algorithm and its model-specific settings differed. The hyperparameter settings for both models are listed in Table S4.

Meteorological normalization was used to estimate O_3 concentrations under resampled meteorological conditions and to distinguish meteorological variability from the meteorologically normalized long-term component, following frameworks used in air-quality studies (Grange et al., 2018; Vu et al., 2019; Dai et al., 2023). For each target date, temporal variables were kept unchanged, while the nine meteorological variables were jointly sampled as a single vector to preserve their joint structure. Specifically, valid records containing all nine meteorological variables were sampled from a circular $\pm$ 14 d window centered on the target date's day of year. For example, for a target date of 15 July, meteorological observations were sampled from 1–29 July across all available years. This approach preserves the seasonal characteristics of meteorology while reducing the influence of year-specific anomalies.

For each target date, the resampled meteorological variables and fixed temporal variables were input into the corresponding trained model (LightGBM or RF) to predict MDA8 O_3. This procedure was repeated 1000 times, and the average of the 1000 predictions was defined as the meteorologically normalized MDA8 O_3 concentration for that date. The normalized concentration represents the mean model-predicted O_3 concentration under average meteorological conditions resampled from the selected seasonal window. Therefore, the difference between the observed and normalized concentrations can be interpreted as the meteorological anomaly contribution, whereas the normalized time series reflects a meteorologically normalized long-term component. This component is a model-based composite signal that may reflect changes in precursor emissions, background O_3, regional transport, natural emissions, and other processes not explicitly represented in the model; it is not a physically isolated estimate of anthropogenic emission changes.

Sensitivity tests were conducted to evaluate the influence of the normalization parameters, including the number of iterations and the sampling window size (Figs. S3 and S4). The variability among repeated meteorological-normalization calculations decreased as the number of predictions increased and became relatively stable at approximately 1000 predictions. Therefore, 1000 iterations were used in the final meteorological normalization procedure. The interannual trends of normalized MDA8 O_3 remained stable when the sampling window varied from $\pm$ 7 to $\pm$ 28 d, indicating that the selected $\pm$ 14 d window provided a reasonable balance between meteorological representativeness and sample size.

For each region and season, O_i and N_i denote the observed and meteorologically normalized annual mean MDA8 O_3 concentrations in year i, respectively. The meteorological contribution in year i is defined as:

$$M_i = O_i - N_i \tag{1}$$

where M_i is the meteorological contribution in year i, O_i is the observed seasonal mean MDA8 O_3 concentration in year i, and N_i is the meteorologically normalized long-term component.

For the change from year i to year j, the observed change is:

$$\Delta O = O_j - O_i \tag{2}$$

The non-meteorological contribution is then defined as:

$$\Delta N_i = \Delta O - M_i \tag{3}$$

Here, ΔN_i represents the part of the observed change not accounted for by M_i and may reflect changes in precursor

emissions, background O_3, regional transport, natural emissions, and other processes not explicitly represented in the model.

2.3 SHapley Additive exPlanations (SHAP) approach

To identify the meteorological variables most strongly associated with MDA8 O_3 variability, we applied the SHapley Additive exPlanations (SHAP) method to the SHAP-specific LightGBM model (Lundberg and Lee, 2017; Lundberg et al., 2020).

SHAP is based on cooperative game theory and decomposes a model prediction into a baseline value and contributions from individual predictors.

For a given prediction, the SHAP representation can be expressed as:

$$f(x) = \varphi_0 + \sum_{i=1}^{M} \varphi_i \tag{4}$$

where $f(x)$ is the LightGBM-predicted MDA8 O_3 concentration for sample x, φ_0 is the baseline model output, defined as the expected prediction over the background dataset, M is the number of input variables, and φ_i is the SHAP value of predictor i. A positive SHAP value indicates that the predictor increases the predicted MDA8 O_3 concentration relative to the baseline, whereas a negative value indicates a decrease. The absolute magnitude of the SHAP value indicates the strength of the model-attributed contribution of that predictor to a specific prediction.

In this study, SHAP values were calculated using a separate LightGBM model (inputs: T2M, SSRD, TCC, BLH, U10, V10, SP, RH, and TP; output: MDA8 O_3; baseline: expected model output; importance metric: mean absolute SHAP value). The SHAP model used the hyperparameters selected for the corresponding site- and season-specific LightGBM model through the validation procedure described in Sect. 2.2 (Table S4). Site-level mean absolute SHAP values were used to identify the most important meteorological variable in each season, while signed SHAP values were aggregated from sites to cities and regions to summarize the annual direction of the modelled meteorological contribution. To assess the sensitivity of variable rankings to the learning algorithm, we also calculated SHAP values for RF models using the same nine meteorological predictors, without temporal variables.

For regional annual analysis, signed SHAP values were first averaged over the available daily records for each site, season, and year. The resulting site-level annual means were then averaged across sites within each city and across cities within each region using equal city weights. Positive and negative values were retained, and the regional annual means of the nine meteorological variables were summed to obtain the annual SHAP total shown by the black line in Figs. 6b and 7b.

This SHAP total is a model-based signed summary and is distinct from the meteorological contribution $M_i = O_i - N_i$ used for comparison. Accordingly, the two are compared only in terms of their regional annual patterns, and their magnitudes are not expected to agree quantitatively. It should be noted that SHAP values describe model-based associations between meteorological predictors and model-predicted MDA8 O_3 concentrations; they do not establish physical causality. We therefore discuss the results in the context of atmospheric processes related to O_3 formation, transport, and dispersion, while recognizing that SHAP analysis does not identify these processes individually.

3 Results and discussion

3.1 Performance of the machine learning model

Figure 1 shows the performance of the LightGBM models in predicting daily MDA8 O_3 concentrations across China during the warm and cold seasons. Model performance was evaluated using held-out test observations for each monitoring site, and the spatial distributions of site-level R^2 are shown in Fig. 1a and b. Density scatter plots of observed and predicted daily MDA8 O_3 concentrations are shown in Fig. 1c and d. Overall, the LightGBM models reproduced the observed daily variability of MDA8 O_3 reasonably well in both seasons, although the model skill varied among regions and monitoring sites.

During the warm season, the mean site-level testing R^2 was 0.62. Based on all available test observations, the RMSE and MAE were 20.9 and 16.4 $\mu g\,m^{-3}$, respectively. During the cold season, the mean site-level testing R^2 was 0.68, and the RMSE and MAE were 18.3 and 14.0 $\mu g\,m^{-3}$, respectively. The observed and predicted values were generally distributed around the 1 : 1 line, indicating that the models captured the main variations in daily MDA8 O_3 in both seasons. To assess whether meteorological normalization results were sensitive to the choice of learning algorithm, we also used RF as an alternative model and evaluated its predictive performance using the same available test observations. RF yielded mean site-level R^2 values of 0.62 and 0.70 in the warm and cold seasons, respectively; pooled RMSE and MAE were 21.1 and 16.6 $\mu g\,m^{-3}$ in the warm season and 18.0 and 13.7 $\mu g\,m^{-3}$ in the cold season (Fig. S5). The comparable performance supports the use of RF as an alternative-model sensitivity check in the subsequent meteorological normalization analysis.

The better model performance in the cold season may be related to weaker photochemical activity and relatively lower variability in O_3 concentrations compared with the warm season. In contrast, warm-season O_3 is more strongly influenced by nonlinear photochemical production, episodic high-temperature events, and regional transport, which may increase the difficulty of prediction. Nevertheless, the testing results indicate that the LightGBM models are able to repre-

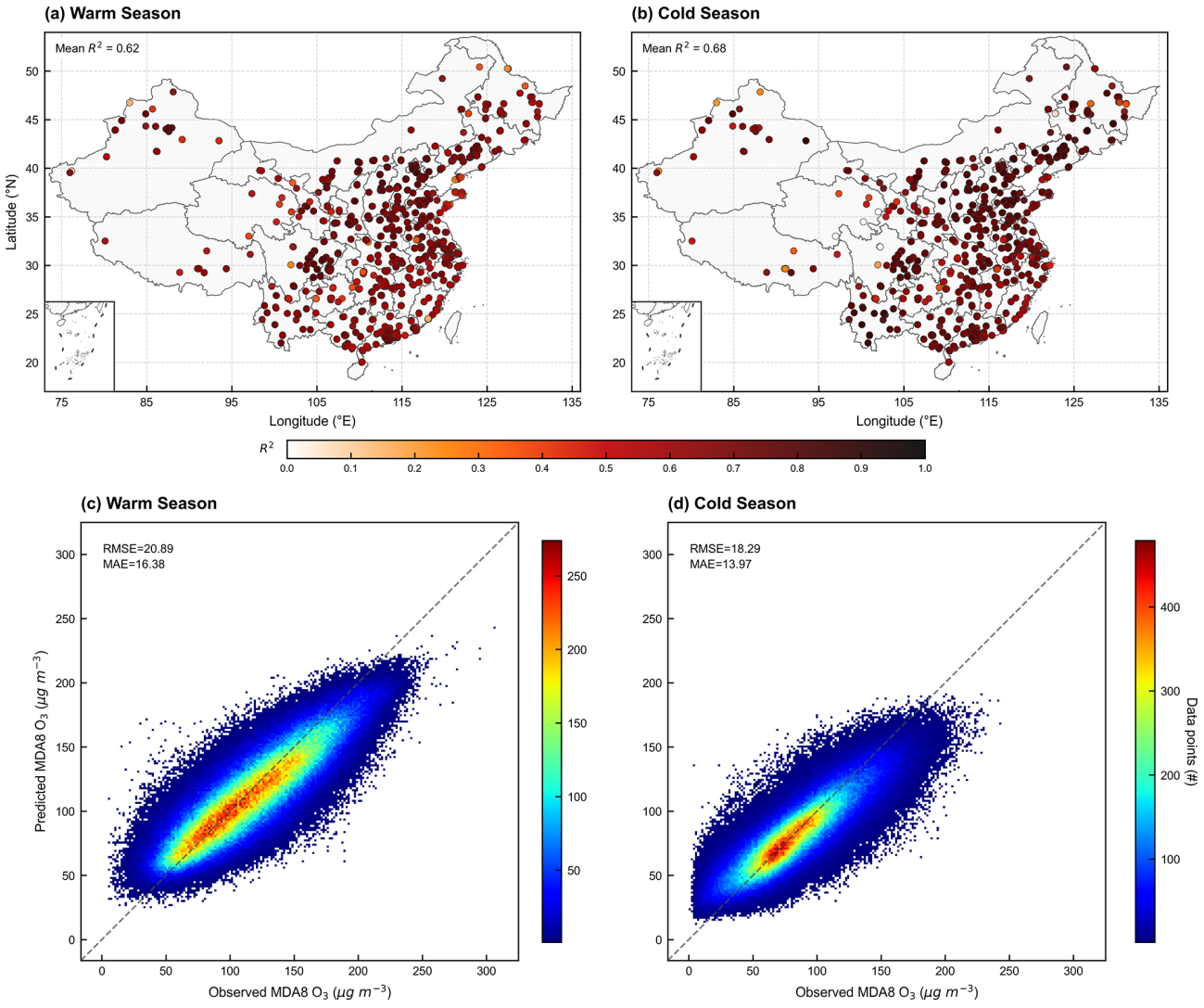


Figure 1. Performance of the LightGBM models for daily MDA8 O_3 prediction. **(a, b)** Spatial distributions of site-level testing R^2 during the warm and cold seasons, respectively. **(c, d)** Density scatter plots of observed versus predicted daily MDA8 O_3 concentrations during the warm and cold seasons, respectively. The dashed lines indicate the 1 : 1 line.

sent the main temporal variability of MDA8 O_3 in both seasons. The model performance is comparable to that reported in recent machine-learning studies of O_3 variability in China (Mao et al., 2024; Wang et al., 2025c; Ye et al., 2026; Chen et al., 2026), providing a reasonable basis for subsequent meteorological normalization and SHAP-based interpretation.

3.2 Spatiotemporal patterns of MDA8 O_3 across China

Figure 2 shows the spatial distributions of mean MDA8 O_3 concentrations across China during the warm and cold seasons from 2015 to 2024. Seasonal differences were evident in both MDA8 O_3 concentration levels and spatial patterns. The warm-season national mean MDA8 O_3 concentration was $110.4 \pm 7.0\,\mu g\,m^{-3}$. Higher mean MDA8 O_3 concentrations occurred mainly in northern and eastern China, with regional clusters in the NCP, FWP, and YRD. The NCP had the highest regional mean MDA8 O_3 concentration ($135.6 \pm 10.4\,\mu g\,m^{-3}$), followed by the FWP ($127.8 \pm 12.9\,\mu g\,m^{-3}$) and the YRD ($124.5 \pm 9.3\,\mu g\,m^{-3}$). Warm-season city mean MDA8 O_3 concentrations exceeded $150\,\mu g\,m^{-3}$ in Dezhou, Dongying, Jinan, and Zhangqiu, all in Shandong Province. These high values may be associated with strong photochemical production under high temperatures and intense solar radiation, together with abundant anthropogenic precursor emissions in highly industrialized and urbanized areas.

Lower warm-season MDA8 O_3 concentrations were mainly found in parts of Southwest and Northeast China. For example, Xishuangbanna and Pu'er in Yunnan Province had mean concentrations of 63.1 and $65.9\,\mu g\,m^{-3}$, respec-

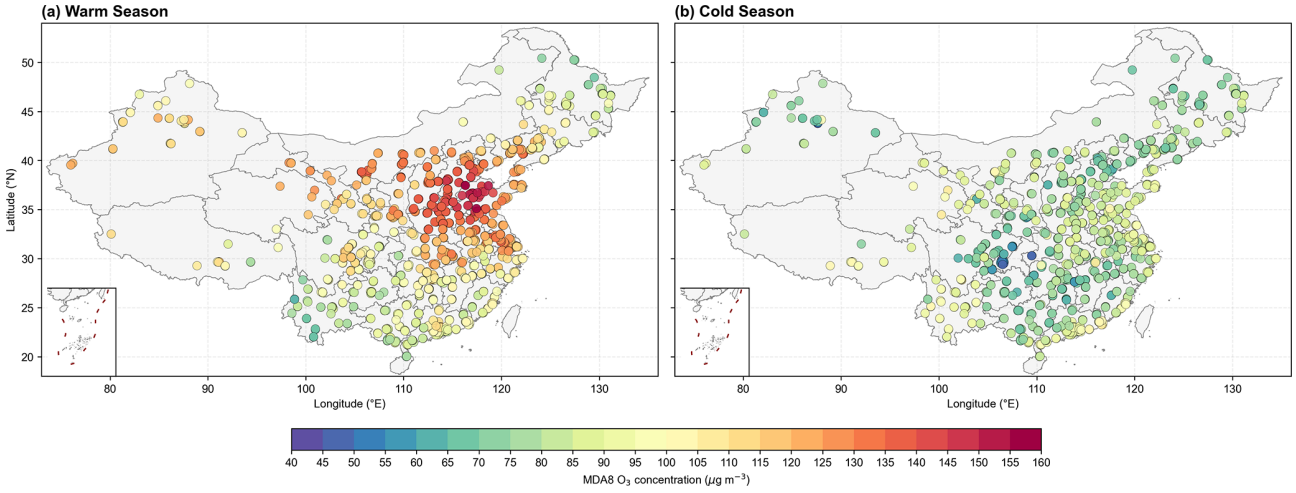


Figure 2. Spatial distributions of mean MDA8 O_3 concentrations across China during 2015–2024. **(a)** Warm season and **(b)** cold season. The warm season is defined as May–October, and the cold season is defined as November–April.

tively, while Yichun in Heilongjiang Province had a mean concentration of 70.4 $\mu g\,m^{-3}$. These relatively low values may be related to weaker photochemical conditions, lower anthropogenic precursor emissions, stronger ventilation, and more frequent cloudy or rainy conditions. Among the key regions, the SCB had a warm-season mean MDA8 O_3 concentration of $104.3 \pm 8.0\,\mu g\,m^{-3}$, while the PRD showed the lowest warm-season level, at $100.6 \pm 7.2\,\mu g\,m^{-3}$. The relatively lower warm-season O_3 in the PRD may reflect the combined effects of monsoonal ventilation, cloudy and rainy conditions, and regional transport processes, consistent with previous studies of O_3 variability in southern China (Li et al., 2020; Cao et al., 2024b).

During the cold season, the national mean MDA8 O_3 concentration decreased to $80.1 \pm 7.2\,\mu g\,m^{-3}$, reflecting the seasonal weakening of photochemical O_3 production. In contrast to the warm-season pattern, higher mean MDA8 O_3 concentrations shifted southward, and the PRD had the highest regional mean among the five key regions ($86.4 \pm 12.0\,\mu g\,m^{-3}$). Shantou had a cold-season mean MDA8 O_3 concentration of 105.3 $\mu g\,m^{-3}$. This spatial pattern may be related to the relatively warm winter climate in southern China, changes in monsoonal transport, and weaker NO titration under changing precursor emissions (Wang et al., 2022b; Cao et al., 2024b). By comparison, the YRD, NCP, FWP, and SCB had lower cold-season mean MDA8 O_3 concentrations of 84.6 ± 8.7, 79.4 ± 7.9, 74.1 ± 10.0, and $69.2 \pm 6.3\,\mu g\,m^{-3}$, respectively. These results indicate a seasonal redistribution of surface MDA8 O_3 concentrations, with higher warm-season values mainly in northern and eastern China and relatively higher cold-season values in southern coastal regions.

Figure 3 further shows the interannual variations in MDA8 O_3 concentrations during the warm and cold seasons from 2015 to 2024. National mean MDA8 O_3 increased significantly in both seasons, with slopes of 2.0 and 2.2 $\mu g\,m^{-3}\,yr^{-1}$ in the warm and cold seasons, respectively ($p < 0.01$). Among the 1142 sites, 88.6 % showed increasing warm-season trends, and 38.7 % of all sites showed significant increases ($p < 0.05$); the corresponding proportions in the cold season were 94.3 % and 52.0 %, respectively. These widespread increases indicate that surface O_3 pollution in China has continued to intensify during the past decade, not only during the photochemically active warm season but also during the cold season.

During the warm season, the national mean MDA8 O_3 concentration increased at a rate of 2.0 $\mu g\,m^{-3}\,yr^{-1}$, rising from $98.3 \pm 11.6\,\mu g\,m^{-3}$ in 2015 to $117.0 \pm 15.5\,\mu g\,m^{-3}$ in 2024, corresponding to a cumulative increase of approximately 19.1 %. This increasing trend is consistent with previous studies reporting sustained O_3 enhancement in China under the combined influence of changing precursor emissions and meteorological variability (Ren et al., 2022; Fang et al., 2026; Goto et al., 2026). Regionally, the FWP showed the strongest warm-season increase, with a trend of 3.4 $\mu g\,m^{-3}\,yr^{-1}$ and a cumulative increase of 44.2 %. By 2024, its regional mean MDA8 O_3 concentration reached $145.2 \pm 32.4\,\mu g\,m^{-3}$. The NCP, YRD, and SCB also showed marked increases, with trends of 2.7, 2.5, and 2.0 $\mu g\,m^{-3}\,yr^{-1}$, respectively. In contrast, the PRD exhibited a more moderate warm-season increase of 1.3 $\mu g\,m^{-3}\,yr^{-1}$ (Wang et al., 2022a; Wu et al., 2022; Zhang et al., 2025). Overall, warm-season O_3 increased more rapidly in northern and inland regions than in southern coastal regions.

Cold-season MDA8 O_3 concentrations also increased nationally, with a trend of 2.2 $\mu g\,m^{-3}\,yr^{-1}$ ($p < 0.01$). The FWP and PRD had similar estimated slopes of 2.9 $\mu g\,m^{-3}\,yr^{-1}$, although the trend was significant in the FWP ($p < 0.01$) but not in the PRD ($p = 0.11$). The NCP,

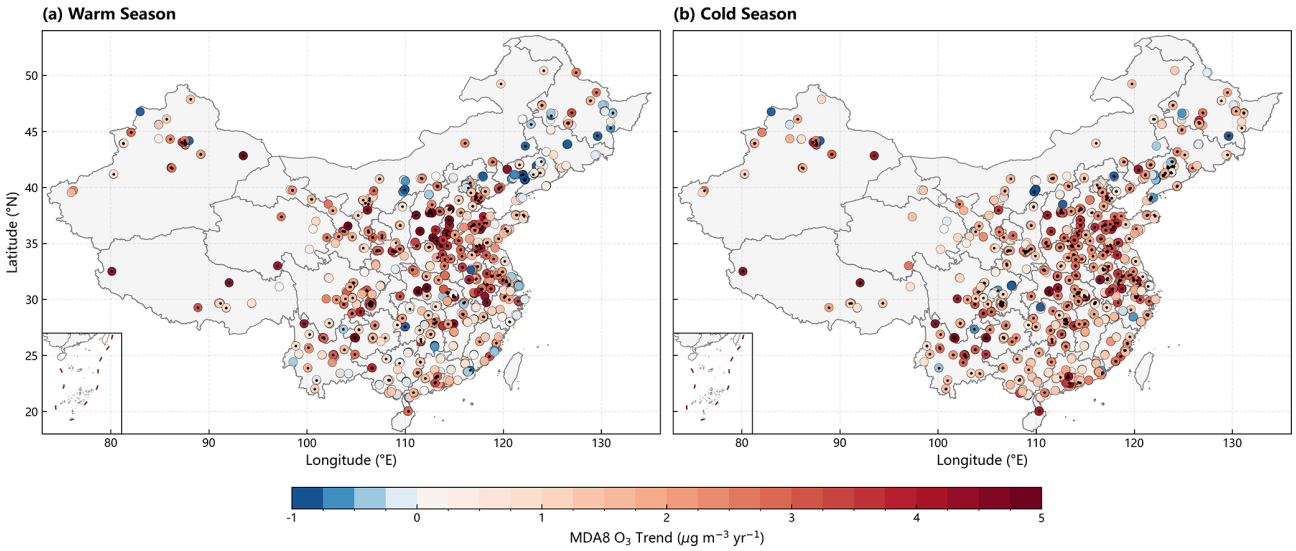


Figure 3. Spatial distributions of interannual trends in MDA8 O_3 concentrations across China from 2015 to 2024. **(a)** Warm-season MDA8 O_3 and **(b)** cold-season MDA8 O_3. Dots indicate statistically significant trends ($p < 0.05$).

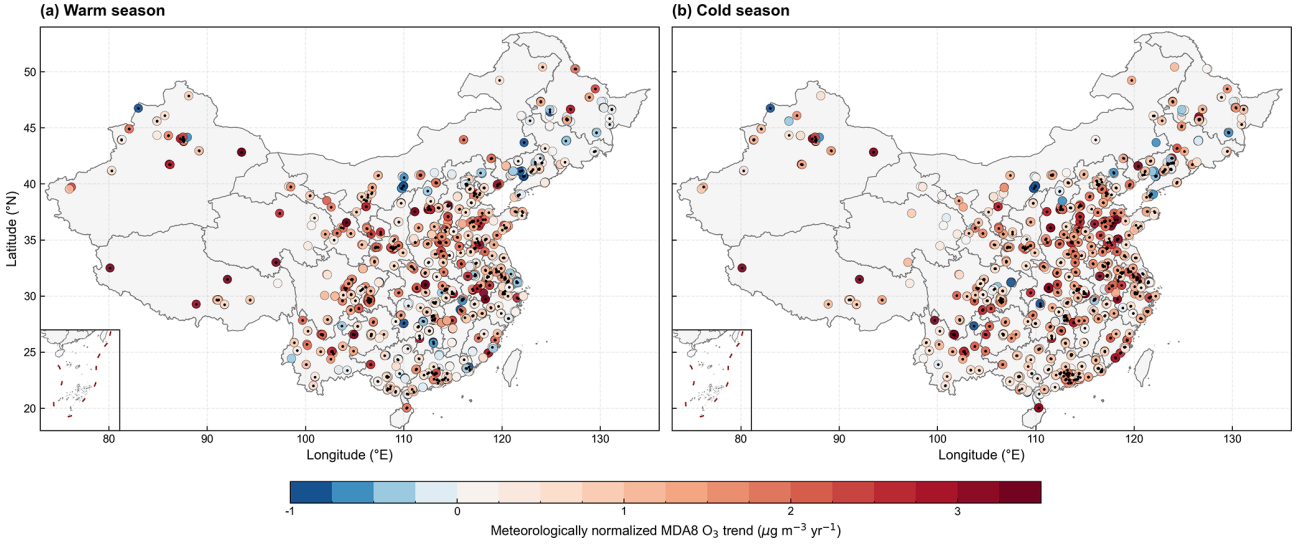


Figure 4. Spatial distributions of trends in meteorologically normalized MDA8 O_3 across China during 2015–2024, where dots denote statistical significance ($p < 0.05$). **(a)** Warm season and **(b)** cold season. Trends were calculated from the meteorologically normalized seasonal mean MDA8 O_3time series at each monitoring site.

YRD, and SCB showed significant increases of 2.3, 2.5, and 1.7 $\mu g\,m^{-3}\,yr^{-1}$, respectively ($p < 0.05$). These results suggest that the recent rise in surface O_3 in China is not limited to the warm season. The cold-season increase may reflect the combined effects of changing precursor emissions, weakened NO titration, background O_3 changes, regional transport, and meteorological variability, highlighting the need to consider season-specific processes in O_3 pollution control (Li et al., 2021; Tong et al., 2023; Cao et al., 2024a).

3.3 Interannual variations in meteorologically normalized MDA8 O_3

Figure 4 shows the spatial distributions of interannual trends in meteorologically normalized MDA8 O_3 during the warm and cold seasons from 2015 to 2024. Positive trends were found at 86.7 % of sites in the warm season and 92.0 % in the cold season. Statistically significant positive trends occurred at 60.0 % and 72.2 % of sites, respectively ($p < 0.05$). The magnitude and significance of the normalized trends varied across China. Meteorological normalization was applied to reduce the influence of short-term and interannual mete-

orological fluctuations and to extract the long-term component of O_3 variability that cannot be explained by meteorology in the model framework. After normalization, MDA8 O_3 still showed increasing trends at the national scale and across most key regions in both seasons, indicating that the observed O_3 increase was not solely driven by meteorological variability.

At the national scale, observed warm-season MDA8 O_3 increased from 98.3 $\mu g\,m^{-3}$ in 2015 to 117.0 $\mu g\,m^{-3}$ in 2024, corresponding to a trend of 2.0 $\mu g\,m^{-3}\,yr^{-1}$ ($p < 0.01$). The meteorologically normalized warm-season MDA8 O_3 increased by 15.1 $\mu g\,m^{-3}$ from 2015 to 2024, with a Theil–Sen slope of 1.1 $\mu g\,m^{-3}\,yr^{-1}$ ($p < 0.001$). The observed increase exceeded the normalized increase by approximately 3.6 $\mu g\,m^{-3}$, indicating that meteorological variability contributed to part of the observed change. The warm-season increase remained evident after meteorological normalization, consistent with previous studies emphasizing the importance of precursor-emission changes and chemical-regime shifts in recent O_3 increases in China (Li et al., 2020; Liu et al., 2023b). Meteorological variability also modulated the observed increase, particularly in years with conditions favorable for photochemical O_3 production (Gao et al., 2023; Meng et al., 2023).

During the cold season, observed MDA8 O_3 also increased substantially, from 66.7 $\mu g\,m^{-3}$ in 2015 to 86.7 $\mu g\,m^{-3}$ in 2024, corresponding to a trend of 2.2 $\mu g\,m^{-3}\,yr^{-1}$ ($p < 0.01$). The meteorologically normalized cold-season MDA8 O_3 increased by 15.8 $\mu g\,m^{-3}$ from 2015 to 2024, with a Theil–Sen slope of 1.2 $\mu g\,m^{-3}\,yr^{-1}$ ($p < 0.001$). The observed increase exceeded the normalized increase by approximately 4.2 $\mu g\,m^{-3}$, indicating that meteorological variability contributed to part of the observed change. The cold-season increase likewise remained evident after meteorological normalization. It is consistent with a weakened NO titration effect under declining NO_x emissions and with changes in background O_3 and regional transport, although these processes cannot be fully separated using meteorological normalization alone (Le et al., 2020; Li et al., 2021; Tong et al., 2023). Meteorological conditions may further influence cold-season O_3 through changes in solar radiation, boundary-layer stability, and ventilation, which affect photochemical production and near-surface accumulation under low-photochemical conditions (Xiang et al., 2019).

At the regional scale, Fig. 5 compares the observed seasonal mean MDA8 O_3 and the interannual changes in the meteorologically normalized series across the five key regions. During the warm season, the normalized series increased significantly in the NCP, YRD, FWP, and SCB, with Theil–Sen slopes of 1.0, 0.9, 1.5, and 1.3 $\mu g\,m^{-3}\,yr^{-1}$, respectively (all $p < 0.01$). The PRD showed a positive but non-significant trend of 0.8 $\mu g\,m^{-3}\,yr^{-1}$ ($p = 0.074$). These regional differences suggest that the meteorologically normalized long-term component of warm-season O_3 increased more rapidly in northern inland and basin regions than in eastern and southern coastal regions. This pattern may be related to regional differences in precursor-emission changes, chemical sensitivity regimes, topographic constraints, and ventilation conditions (Yang et al., 2019; Liu et al., 2023b).

The normalized warm-season MDA8 O_3 series also showed year-to-year variation: it increased during 2015–2019, showed a short-term slowdown or decline around 2020 in several regions, and generally increased again during 2021–2024. The change around 2020 may reflect short-term perturbations in emissions and atmospheric chemistry associated with the COVID-19 period, together with interannual variability in meteorological and regional transport conditions. The meteorologically normalized long-term component still includes multiple non-meteorological processes and should therefore not be treated as a quantitative measure of emission reductions.

During the cold season, meteorologically normalized MDA8 O_3 increased significantly in all five key regions (all $p < 0.01$), but the regional pattern differed from that of the warm season. The cold-season normalized trends were higher than the corresponding warm-season trends in the NCP, YRD, PRD, and FWP. The FWP showed the largest cold-season normalized increase, with a slope of 2.0 $\mu g\,m^{-3}\,yr^{-1}$, followed by the NCP at 1.5 $\mu g\,m^{-3}\,yr^{-1}$. The YRD and PRD both increased at 1.3 $\mu g\,m^{-3}\,yr^{-1}$, whereas the SCB showed a lower cold-season slope of 0.6 $\mu g\,m^{-3}\,yr^{-1}$. The magnitude of the normalized O_3 increase therefore varied by both region and season. To examine whether the cold-season increase was concentrated in March–April, we analysed monthly trends in meteorologically normalized MDA8 O_3 (Fig. S6 and Sect. S3). Meteorologically normalized MDA8 O_3 increased in every cold-season month nationally and in all five regions ($p < 0.05$), indicating that the increase extended beyond the spring months. The cold-season mean trend reflects an overall increase, but the rates of increase varied among months and regions.

These trends were estimated using LightGBM-based meteorological normalization, and the choice of learning algorithm may also affect their magnitude and statistical significance. To assess the sensitivity of the regional seasonal patterns in Fig. 5 to model choice, we also compared the results with those obtained using RF. The RF analysis is broadly reproduced the patterns identified with LightGBM (Table S5, Fig. S7 and Sect. S4). Both models estimated the largest normalized trends in the FWP in both seasons and the weakest cold-season trend in the SCB. The main difference in statistical significance occurred for the PRD warm-season trend: the RF estimate was significant (0.7 $\mu g\,m^{-3}\,yr^{-1}$, $p < 0.001$), whereas the similar LightGBM estimate (0.8 $\mu g\,m^{-3}\,yr^{-1}$) was not ($p = 0.074$). Annual normalized concentrations also differed between the models. Overall, the increase remained evident after meteorological normalization in both seasons, while meteorological variability contributed to the interannual variation in observed O_3. Differences between the two

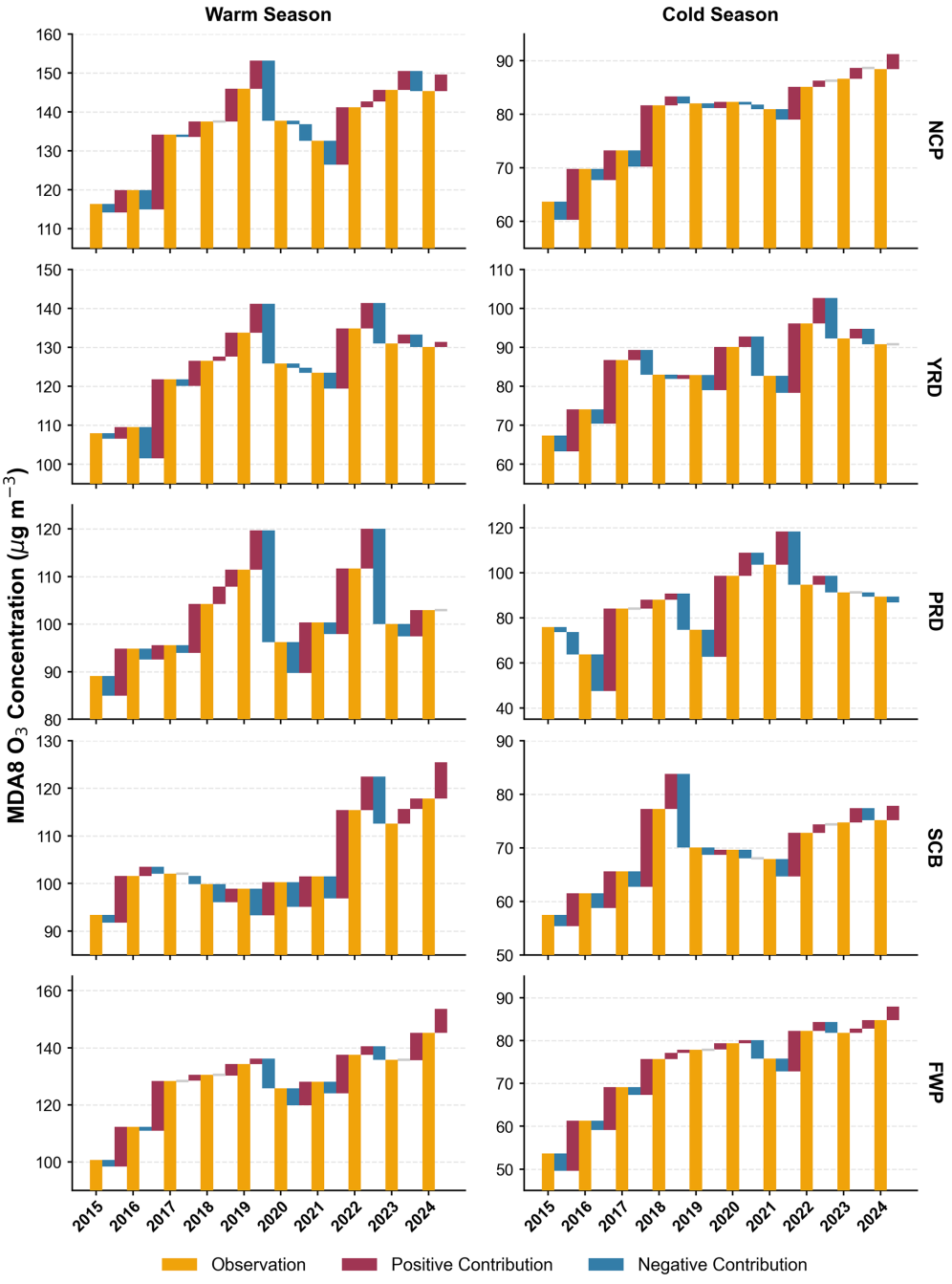


Figure 5. Regional mean MDA8 O_3 concentrations and their year-to-year decomposition in the five key regions during 2015–2024. The left and right columns show the warm and cold seasons, respectively. Orange bars show the observed concentration for each year (O_i); the two bars following each orange bar show the changes in the meteorological component (M_i) and the meteorologically normalized long-term component (ΔN_i) from that year to the next (Sect. 2.2). Red and blue indicate positive and negative changes, respectively.

models indicate some uncertainty in the magnitude of the normalized changes. These results highlight the need to address cold-season O_3 increases alongside warm-season pollution, with priorities varying by region.

3.4 SHAP-based interpretation of meteorological influences on O_3

The meteorological normalization analysis showed that the long-term increase in MDA8 O_3 remained evident after meteorological resampling, while meteorological variability modulated the magnitude and interannual fluctuations of O_3.

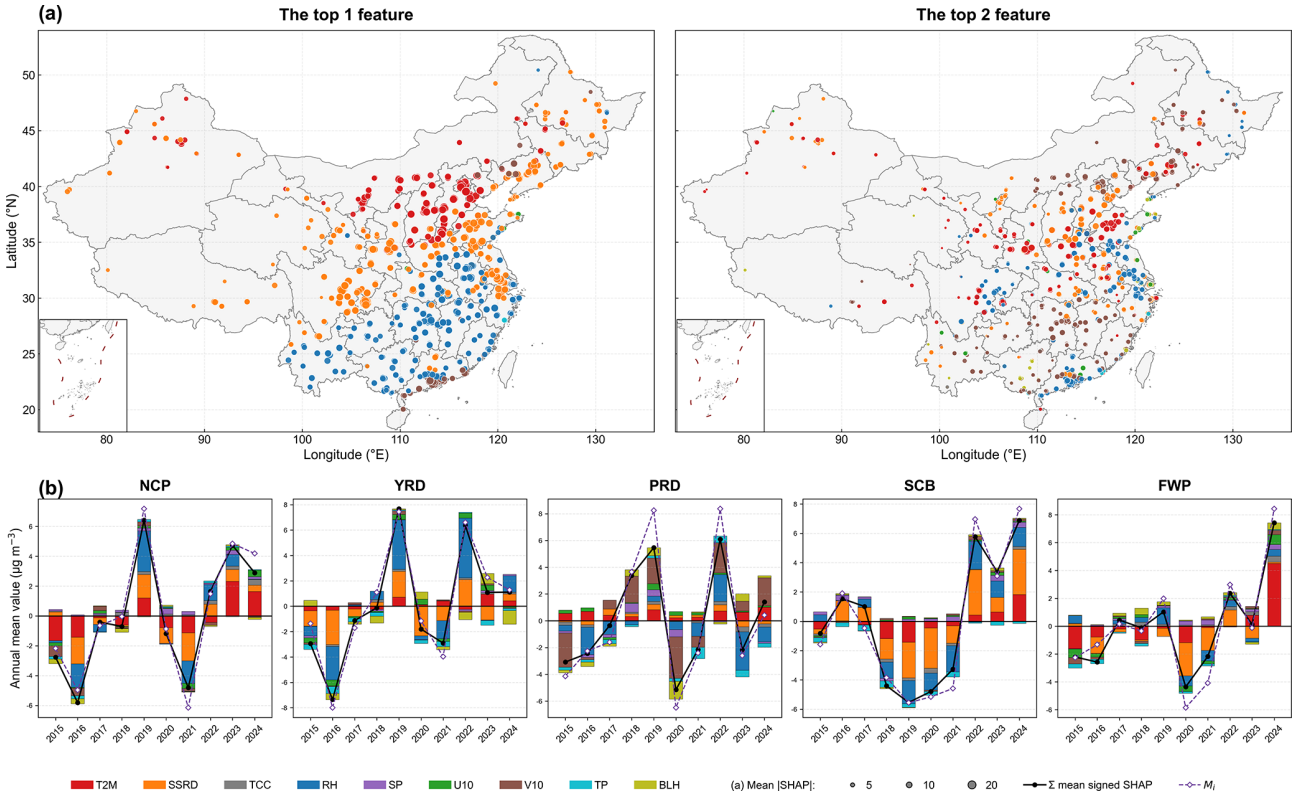


Figure 6. SHAP-based interpretation of warm-season meteorological influences on MDA8 O_3 during 2015–2024. **(a)** Spatial distributions of the two leading meteorological variables at monitoring sites. Colors indicate different meteorological variables, and marker sizes indicate the corresponding mean absolute SHAP values. **(b)** Regional annual mean signed SHAP values for the nine meteorological variables. Colored bars represent individual variables. In panel **(b)**, black lines show the sum of the regional annual mean signed SHAP values for the nine meteorological variables, and purple dashed lines show $M_i = O_i - N_i$ from the meteorological normalization analysis for qualitative comparison.

To examine the meteorological variables most strongly associated with O_3 variability, we applied SHAP analysis to separate LightGBM models trained using the nine meteorological predictors, as described in Sect. 2.3. Figures 6a and 7a show the two highest-ranked variables at each site based on mean absolute SHAP values; marker size indicates the corresponding value, whereas the site percentages reported below refer to the highest-ranked variable. Figures 6b and 7b show regional annual mean signed SHAP values for the individual variables, with the black line representing their sum and the purple dashed line representing $M_i = O_i - N_i$ for qualitative comparison of their regional annual patterns.

Figure 6a shows the spatial distribution of the two leading meteorological variables for warm-season MDA8 O_3. At the national scale, SSRD, RH, and T2M were the most frequently identified dominant variables, accounting for 41.4 %, 34.8 %, and 16.7 % of monitoring sites, respectively. This indicates that warm-season O_3 variability in the model was mainly associated with radiative, moisture, and thermal conditions. The dominant variables showed clear spatial heterogeneity. In northern inland and basin regions, such as the NCP, FWP, and SCB, O_3 variability was more strongly associated with temperature and radiation. In the NCP, T2M was the dominant variable at 51.4 % of monitoring sites, with a mean absolute SHAP value of 17.7 $\mu g\,m^{-3}$ among these sites. In the FWP and SCB, SSRD was the dominant variable at 64.4 % and 98.6 % of monitoring sites, respectively, with corresponding mean absolute SHAP values of 17.4 and 16.6 $\mu g\,m^{-3}$ among these sites.

The prominence of T2M and SSRD in these northern and basin regions is consistent with the role of high temperature and strong solar radiation in enhancing photochemical O_3 production during the warm season. High temperatures can accelerate photochemical reaction rates and may also enhance biogenic VOC emissions, while strong solar radiation promotes photolysis reactions that initiate O_3 formation (Wang et al., 2024). In basin regions such as the SCB and FWP, topographic constraints and relatively stagnant conditions may further favor O_3 accumulation when photochemical production is strong. These spatial patterns reflect model-attributed associations, and distinguishing the effects of precursor emissions, chemistry, and transport would require additional chemical observations or process-based modelling.

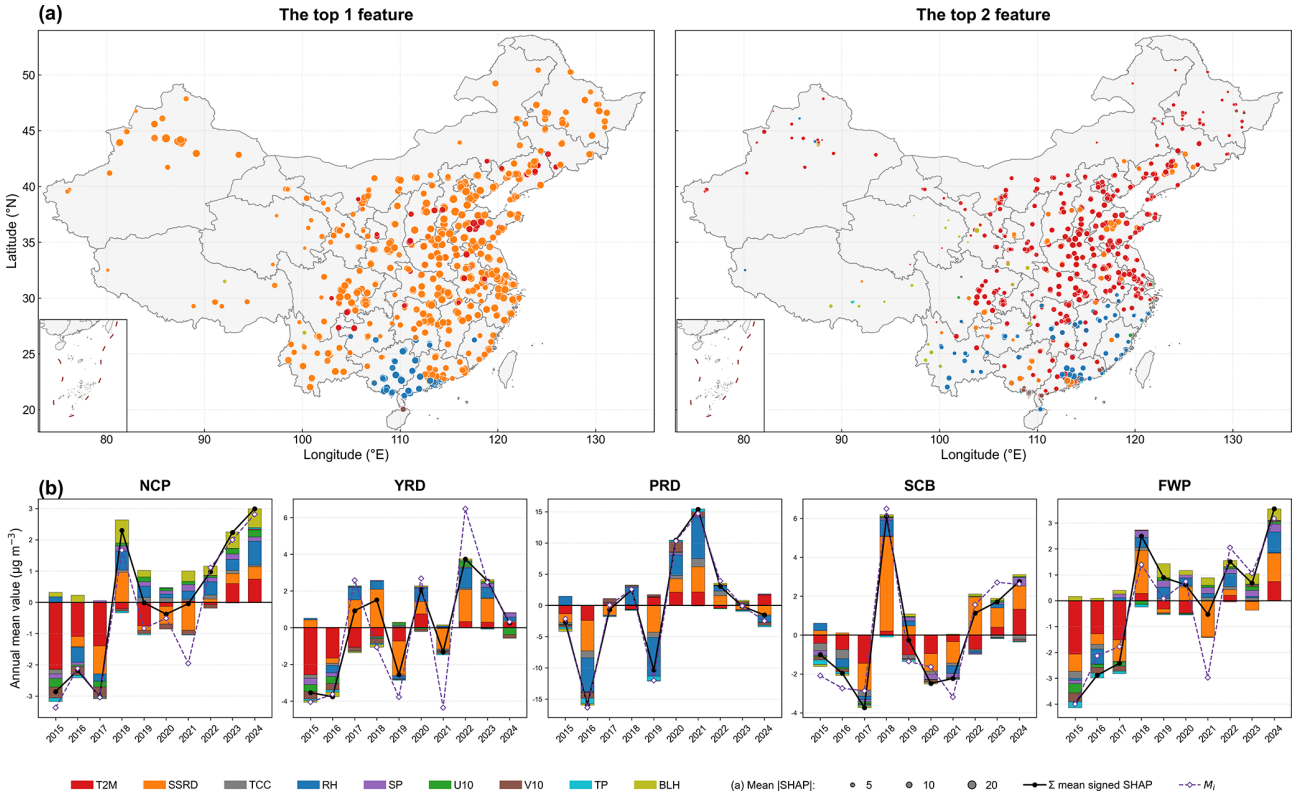


Figure 7. As in Fig. 6, but for the cold season.

Warm-season SHAP results for the YRD and PRD both highlighted RH, although the other leading variable differed between the two regions. In the YRD, SSRD and RH were identified as the dominant variables, accounting for 56.6 % and 43.4 %, respectively, with corresponding mean absolute SHAP values of 15.1 and 12.9 $\mu g\,m^{-3}$. In the PRD, RH and V10 were identified as dominant at similar proportions (49.0 % and 47.1 %), with mean absolute SHAP values of 13.7 and 15.3 $\mu g\,m^{-3}$, respectively. Overall, the SHAP results associate warm-season O_3 variability in these coastal regions with radiation, moisture, and circulation. Regional differences in warm-season coastal O_3 variability may be related to differences in humid monsoonal air masses, cloudiness, and regional ventilation. High RH can occur alongside cloudy conditions, under which reduced solar radiation may limit photochemical O_3 production. The RH association may also reflect other covarying meteorological conditions, such as atmospheric mixing. V10 is the meridional wind component, and its association with O_3 may relate to regional transport and ventilation. A previous study in the coastal city of Shenzhen also reported associations of humidity and regional wind fields with O_3 variability (Mai et al., 2024).

Figure 6b shows substantial interannual variation in the warm-season SHAP sums. Values were generally negative during 2015–2018 and became positive in most regions in 2019, before returning to negative values across all five regions in 2020–2021. Positive sums were more widespread after 2021, although the PRD showed a negative sum in 2023. In 2024, all five regions had positive sums. The largest sum occurred in the FWP (7.4 $\mu g\,m^{-3}$), where T2M contributed 4.5 $\mu g\,m^{-3}$. The SCB had a similarly large sum of 6.9 $\mu g\,m^{-3}$, but its largest positive component was SSRD (3.1 $\mu g\,m^{-3}$). The normalization-based (M_i) series broadly followed the year-to-year variation in the SHAP sums, although their magnitudes and, in some region–year pairs, their signs differed. The comparison suggests similar features of annual meteorological variability, while the different reference baselines and calculation procedures mean that the two quantities are not directly equivalent.

Figure 7a shows the spatial distribution of the two leading meteorological variables for cold-season MDA8 O_3, based on mean absolute SHAP values. Compared with the warm season, SSRD was more frequently identified as the dominant model-attributed variable, accounting for 84.5 % of sites nationwide. T2M and RH were dominant at 7.6 % and 7.4 % of sites, respectively. These results show the widespread importance of SSRD in the cold-season models.

The PRD differed from the other four regions in the prominence of RH alongside SSRD. SSRD and RH were identified as dominant variables at 68.6 % and 31.4 % of sites, respectively. Their mean absolute SHAP values, averaged across sites where each variable was dominant, were 14.1

and 11.7 $\mu g\,m^{-3}$, respectively. The prominence of RH may reflect covariation with cloud cover, solar radiation, and air mass characteristics.

Figure 7b follows the same format as Fig. 6b and shows the cold-season results. Summed SHAP values were negative in all five regions in 2015–2016, reaching $-16.0\,\mu g\,m^{-3}$ in the PRD in 2016. In 2018, all five regional sums were positive, ranging from 1.5 to 6.1 $\mu g\,m^{-3}$, with the highest value in the SCB. Regional patterns diverged in 2019–2021: the PRD sums were positive in 2020 and 2021 (10.5 and 15.4 $\mu g\,m^{-3}$), while those in the NCP and SCB remained negative. All five sums were positive again in 2022 (1.0–3.7 $\mu g\,m^{-3}$). In 2024, the PRD sum was $-1.5\,\mu g\,m^{-3}$, whereas the other four regions had positive sums (0.3–3.5 $\mu g\,m^{-3}$). Overall, the cold-season SHAP sums showed marked interannual variability and regional heterogeneity, particularly in the PRD. The prominence of SSRD in Fig. 7a is consistent with this pattern. Although photochemical production is generally suppressed under low-temperature and low-radiation conditions, interannual changes in solar radiation may still affect O_3 production and accumulation (Li et al., 2026). The signs of M_i and the summed SHAP values agreed in most region–year pairs, differing only in the PRD in 2017 and the YRD in 2018.

In the PRD, RH remained among the more important variables in the cold-season model, and its signed SHAP contribution changed direction across years. This indicates that the modelled association between humidity and predicted MDA8 O_3 varied over time rather than remaining fixed. The regional M_i series showed a broadly similar interannual pattern to the summed SHAP series, providing complementary evidence of interannual meteorological modulation in the PRD. Because M_i summarizes the observed–normalized difference whereas the RH SHAP value describes the model association of a single predictor, this comparison is qualitative and does not isolate a specific physical pathway.

Overall, SHAP analysis reveals clear seasonal and regional differences in the meteorological variables associated with MDA8 O_3 variability. During the warm season, temperature and radiation were more prominent in the northern and basin regions; in the YRD, RH was prominent alongside SSRD, whereas in the PRD, RH was prominent alongside V10. During the cold season, SSRD dominated most regions, while RH was also prominent in the PRD, where its regional annual mean signed SHAP contribution was negative in 2019 and positive in 2021. The summed SHAP values and M_i showed broadly similar interannual patterns across the five regions, offering a complementary view of annual meteorological variability, although some region–year differences remained. This comparison is qualitative, given the different reference baselines, aggregation pathways, and daily support of the two series.

To examine whether these seasonal and regional patterns were retained with a different learning algorithm, we compared the LightGBM SHAP results with those from RF (Figs. S8, S9 and Sect. S5). Both models identified broadly similar leading meteorological variables. The first-ranked variable agreed between models at 92.0 % of sites in the warm season and 95.4 % in the cold season; agreement for the second-ranked variable was 76.2 % and 89.0 %, respectively. These percentages denote the proportion of sites with results from both models at which the same variable occupied the corresponding rank. During the warm season, both models most frequently identified T2M as the leading variable in the NCP and SSRD in the YRD, SCB, and FWP. In the PRD, however, RH was most often ranked first by LightGBM and V10 by RF. During the cold season, SSRD was the most frequent leading variable in all five regions in both models, while T2M was most often second in the NCP, YRD, SCB, and FWP and RH in the PRD. These comparisons support the main seasonal and regional patterns in variable importance, although some variable rankings differed between models.

3.5 Uncertainty analysis

Several limitations should be considered when interpreting the results. First, station observations were incomplete during the boundary period of the first cold season (November–December 2014), so some MDA8 O_3 values had to be estimated, introducing uncertainty into the concentration estimates for this period. A second limitation is the lack of long-term, spatially consistent observations of O_3 precursors, particularly VOCs and NO_x, across China. We therefore did not include precursor concentrations or emissions as direct predictors. The meteorologically normalized long-term component is a model-based signal and should not be interpreted as a quantitative estimate of anthropogenic emission changes alone. It may also reflect changes in chemical sensitivity, biogenic VOCs, background O_3, regional transport, and other slowly varying factors not represented in the model. The meteorological input introduces another source of uncertainty. ERA5 provides continuous fields, but its $0.25° \times 0.25°$ grid may miss local conditions around monitoring sites, especially in complex terrain, coastal areas, and densely urbanized regions. Urban heat islands, land-sea breezes, mountain-valley circulations, and local boundary-layer variations may therefore be underrepresented. This limitation is particularly relevant to short-lived or localized high-O_3 episodes.

The normalization also depends on the fitted machine-learning model. It assumes that the LightGBM model can represent the relationships between O_3, temporal predictors, and meteorological variables over the study period. Temporal predictors help describe long-term and seasonal patterns, but they cannot separate anthropogenic emissions, natural emissions, background O_3, and regional transport. The SHAP analysis used models with meteorological predictors only. The resulting SHAP values describe how these predictors contribute to model predictions, rather than direct physical or causal effects. Interpretation also needs to account for relationships among the predictors. Potential correlations

among RH, TCC, SSRD, and TP may influence the relative SHAP values of these variables. The sensitivity analyses using RF further showed that the main regional and seasonal patterns were generally consistent across the two algorithms, although some differences remained in normalized trends and SHAP contributions (Sects. S4 and S5).

Finally, this study uses observational and statistical attribution. It can describe broad spatial and seasonal patterns, but it cannot resolve individual chemical mechanisms or source contributions. Longer precursor records, updated emission inventories, chemical transport models, and causal analyses would be needed to further constrain these processes.

4 Conclusions

In this study, we used LightGBM-based meteorological normalization and SHAP analysis of meteorological predictors to examine the interannual variability of MDA8 O_3 across China during the warm and cold seasons from 2015 to 2024. The results show that surface O_3 increased widely across China in both seasons. The observed national mean MDA8 O_3 increased by $2.0\,\mu g\,m^{-3}\,yr^{-1}$ during the warm season and by $2.2\,\mu g\,m^{-3}\,yr^{-1}$ during the cold season, indicating that recent O_3 enhancement in China is not confined to photochemically active months.

After meteorological normalization, the national mean MDA8 O_3 continued to increase, with slopes of $1.1\,\mu g\,m^{-3}\,yr^{-1}$ in the warm season and $1.2\,\mu g\,m^{-3}\,yr^{-1}$ in the cold season. This indicates that meteorological variability alone does not fully account for the observed increase. The normalized series may reflect the combined influence of precursor-emission changes, background O_3, regional transport, natural emissions, and other processes not explicitly represented in the model; it should therefore not be interpreted as a quantitative estimate of anthropogenic emission changes.

Trends in the meteorologically normalized long-term component showed clear seasonal and regional differences. Among the five regions, the FWP had the largest normalized trend slope in both seasons, whereas the SCB had the smallest cold-season slope. Cold-season slopes were higher than warm-season slopes in the NCP, YRD, PRD, and FWP, while the warm-season slope was higher in the SCB. In particular, the significant cold-season increase in the PRD suggests that future control strategies should also consider cold-season O_3 enhancement in this part of southern coastal China.

SHAP analysis showed seasonal and regional differences in the meteorological variables associated with MDA8 O_3 variability. During the warm season, temperature and radiation were prominent in the NCP, FWP, and SCB, while RH was also prominent in both coastal regions, alongside SSRD in the YRD and V10 in the PRD. During the cold season, SSRD was the most frequently identified dominant variable in each of the five regions. In the PRD, RH was also prominent. At the regional annual scale, the summed SHAP values and M_i showed broadly similar interannual patterns, providing a complementary view of meteorological variability. This comparison is qualitative, given their different reference baselines, aggregation methods, and daily coverage.

Overall, this study highlights the importance of accounting for meteorological variability when interpreting long-term O_3 changes. Meteorological normalization and SHAP analysis provide complementary information on persistent O_3 increases and the meteorological variables associated with O_3 variability. The results emphasize the need to address cold-season O_3 increases alongside warm-season pollution and to account for region-specific meteorological patterns in O_3 control planning.

Data availability. Hourly surface O_3 observations were obtained from the China National Environmental Monitoring Centre (http://www.cnemc.cn/en, last access: 19 April 2026). ERA5 reanalysis data were obtained from the European Centre for Medium-Range Weather Forecasts Reanalysis v5 dataset (https://cds.climate.copernicus.eu/, last access: 19 April 2026).

Supplement. The supplement related to this article is available online at https://doi.org/10.5194/acp-26-15291-2026-supplement.

Author contributions. ZY and RL designed the research; ZY analyzed the data; ZY and RL wrote the original draft; ZY, RL, GC, MW, and TH reviewed and edited the manuscript.

Competing interests. The contact author has declared that none of the authors has any competing interests.

Disclaimer. Publisher's note: Copernicus Publications remains neutral with regard to jurisdictional claims made in the text, published maps, institutional affiliations, or any other geographical representation in this paper. The authors bear the ultimate responsibility for providing appropriate place names. Views expressed in the text are those of the authors and do not necessarily reflect the views of the publisher.

Acknowledgements. We acknowledge the China National Environmental Monitoring Centre and the European Centre for Medium-Range Weather Forecasts for providing datasets that made this work possible. We also acknowledge the support of the College of Environment and Climate, Institute for Environmental and Climate Research, Jinan University.

Financial support. This research has been supported by the National Key Research and Development Program of China (grant no. 2023YFC3706204).

Review statement. This paper was edited by Stefano Galmarini and reviewed by two anonymous referees.

References

Belachsen, I. and Broday, D. M.: Imputation of missing $PM_{2.5}$ observations in a network of air quality monitoring stations by a new kNN method, Atmosphere, 13, 1934, https://doi.org/10.3390/atmos13111934, 2022.

Cao, T., Wang, H., Chen, X., Li, L., Lu, X., Lu, K., and Fan, S.: Rapid increase in spring ozone in the Pearl River Delta, China during 2013–2022, npj Clim. Atmos. Sci., 7, 309, https://doi.org/10.1038/s41612-024-00847-3, 2024a.

Cao, T., Wang, H., Li, L., Lu, X., Liu, Y., and Fan, S.: Fast spreading of surface ozone in both temporal and spatial scale in Pearl River Delta, J. Environ. Sci., 137, 540–552, https://doi.org/10.1016/j.jes.2023.02.025, 2024b.

Chen, C., Li, T., Sun, Q., Shi, W., He, M. Z., Wang, J., Liu, J., Zhang, M., Jiang, Q., Wang, M., and Shi, X.: Short-term exposure to ozone and cause-specific mortality risks and thresholds in China: evidence from nationally representative data, 2013–2018, Environ. Int., 171, 107666, https://doi.org/10.1016/j.envint.2022.107666, 2023.

Chen, L., Lin, J., Xu, J., Kong, H., Weng, H., Zhang, Y., Yun, X., and Tao, S.: Chemically enhanced transboundary ozone pollution suppresses city-level emission control benefits, Environ. Res. Lett., 20, 054009, https://doi.org/10.1088/1748-9326/adc1e1, 2025.

Chen, Y., Dai, Z., Wang, X., Zhang, Q., Chen, H., Zhong, S., Lu, Q., and Yu, L.: Meteorological and socioeconomic impacts on ozone in China: past and future analysis, iScience, 29, 114335, https://doi.org/10.1016/j.isci.2025.114335, 2026.

Dai, Q., Dai, T., Hou, L., Li, L., Bi, X., Zhang, Y., and Feng, Y.: Quantifying the impacts of emissions and meteorology on the interannual variations of air pollutants in major Chinese cities from 2015 to 2021, Sci. China Earth Sci., 66, 1725–1737, https://doi.org/10.1007/s11430-022-1128-1, 2023.

Ding, J., Dai, Q., Fan, W., Lu, M., Zhang, Y., Han, S., and Feng, Y.: Impacts of meteorology and precursor emission change on O_3 variation in Tianjin, China from 2015 to 2021, J. Environ. Sci., 126, 506–516, https://doi.org/10.1016/j.jes.2022.03.010, 2023.

Fang, J., Zhang, Y., Hauglustaine, D., Zheng, B., Wang, M., Li, J., Sun, Y., Li, H., Wang, J., Wu, Y., Yuan, B., Chen, M., and Ge, X.: Tracking surface ozone responses to clean air actions under a warming climate in China using machine learning, Atmos. Chem. Phys., 26, 851–867, https://doi.org/10.5194/acp-26-851-2026, 2026.

Feng, Z., Hu, E., Wang, X., Jiang, L., and Liu, X.: Ground-level O_3 pollution and its impacts on food crops in China: a review, Environ. Pollut., 199, 42–48, https://doi.org/10.1016/j.envpol.2015.01.016, 2015.

Gao, M., Wang, F., Ding, Y., Wu, Z., Xu, Y., Lu, X., Wang, Z., Carmichael, G. R., and McElroy, M. B.: Large-scale climate patterns offer preseasonal hints on the co-occurrence of heat wave and O_3 pollution in China, P. Natl. Acad. Sci. USA, 120, e2218274120, https://doi.org/10.1073/pnas.2218274120, 2023.

Gong, C., Yue, X., Liao, H., and Ma, Y.: A humidity-based exposure index representing ozone damage effects on vegetation, Environ. Res. Lett., 16, 044030, https://doi.org/10.1088/1748-9326/abecbb, 2021.

Goto, D., Yashiro, H., Yamashita, Y., Takigawa, M., Sudo, K., Uchida, J., Yumimoto, K., and Takemura, T.: Assessment of the impacts of anthropogenic ozone precursors on domestic and transboundary ozone concentrations using a high-resolution global chemistry model, Prog. Earth Planet. Sci., 13, 3, https://doi.org/10.1186/s40645-025-00791-7, 2026.

Grange, S. K. and Carslaw, D. C.: Using meteorological normalisation to detect interventions in air quality time series, Sci. Total Environ., 653, 578–588, https://doi.org/10.1016/j.scitotenv.2018.10.344, 2019.

Grange, S. K., Carslaw, D. C., Lewis, A. C., Boleti, E., and Hueglin, C.: Random forest meteorological normalisation models for Swiss PM_{10} trend analysis, Atmos. Chem. Phys., 18, 6223–6239, https://doi.org/10.5194/acp-18-6223-2018, 2018.

Guo, Y., Li, K., Zhao, B., Shen, J., Bloss, W. J., Azzi, M., and Zhang, Y.: Evaluating the real changes of air quality due to clean air actions using a machine learning technique: results from 12 Chinese mega-cities during 2013–2020, Chemosphere, 300, 134608, https://doi.org/10.1016/j.chemosphere.2022.134608, 2022.

He, C., Wu, Q., Li, B., Liu, J., Gong, X., and Zhang, L.: Surface ozone pollution in China: trends, exposure risks, and drivers, Front. Public Health, 11, 1131753, https://doi.org/10.3389/fpubh.2023.1131753, 2023.

Ke, G., Meng, Q., Finley, T., Wang, T., Chen, W., Ma, W., Ye, Q., and Liu, T.-Y.: LightGBM: a highly efficient gradient boosting decision tree, in: NIPS'17: Proceedings of the 31st International Conference on Neural Information Processing Systems, Curran Associates, Inc., 3149–3157, 2017.

Le, T., Wang, Y., Liu, L., Yang, J., Yung, Y. L., Li, G., and Seinfeld, J. H.: Unexpected air pollution with marked emission reductions during the COVID-19 outbreak in China, Science, 369, 702–706, https://doi.org/10.1126/science.abb7431, 2020.

Li, J., Yang, W., Wang, Z., Chen, H., Hu, B., Li, J., Sun, Y., Fu, P., and Zhang, Y.: Modeling study of surface ozone source-receptor relationships in East Asia, Atmos. Res., 167, 77–88, https://doi.org/10.1016/j.atmosres.2015.07.010, 2016.

Li, J., Yu, S., Chen, X., Zhang, Y., Li, M., Li, Z., Song, Z., Liu, W., Li, P., Xie, M., and Xing, J.: Evaluation of the WRF-CMAQ model performances on air quality in China with the impacts of the observation nudging on meteorology, Aerosol Air Qual. Res., 22, 220023, https://doi.org/10.4209/aaqr.220023, 2022.

Li, K., Jacob, D. J., Shen, L., Lu, X., De Smedt, I., and Liao, H.: Increases in surface ozone pollution in China from 2013 to 2019: anthropogenic and meteorological influences, Atmos. Chem. Phys., 20, 11423–11433, https://doi.org/10.5194/acp-20-11423-2020, 2020.

Li, K., Jacob, D. J., Liao, H., Qiu, Y., Shen, L., Zhai, S., Bates, K. H., Sulprizio, M. P., Song, S., Lu, X., Zhang, Q., Zheng, B., Zhang, Y., Zhang, J., Lee, H. C., and Kuk, S. K.: Ozone pollution in the North China Plain spreading into the late-winter haze season, P. Natl. Acad. Sci. USA, 118, e2015797118, https://doi.org/10.1073/pnas.2015797118, 2021.

Li, Y., Li, C., Li, Y., Wang, T., Li, M., Qu, Y., Wu, H., Xie, M., and Wang, Y.: Decadal evolution of aerosol-mediated ozone responses in Eastern China under clean air actions and car-

bon neutrality policies, Atmos. Chem. Phys., 26, 1301–1319, https://doi.org/10.5194/acp-26-1301-2026, 2026.

Liu, J., Wang, L., Li, M., Liao, Z., Sun, Y., Song, T., Gao, W., Wang, Y., Li, Y., Ji, D., Hu, B., Kerminen, V.-M., Wang, Y., and Kulmala, M.: Quantifying the impact of synoptic circulation patterns on ozone variability in northern China from April to October 2013–2017, Atmos. Chem. Phys., 19, 14477–14492, https://doi.org/10.5194/acp-19-14477-2019, 2019.

Liu, Q. and Hang, T.: Seasonal synergistic management of urban heat island effect and $PM_{2.5}$ pollution: insights from interpretable LightGBM-SHAP machine learning model, Environ. Impact Assess. Rev., 116, 108129, https://doi.org/10.1016/j.eiar.2025.108129, 2026.

Liu, X., Gao, H., Zhang, X., Zhang, Y., Yan, J., Niu, J., and Chen, F.: Driving forces of meteorology and emission changes on surface ozone in the Huaihe River Basin, China, Water Air Soil Pollut., 234, 355, https://doi.org/10.1007/s11270-023-06345-1, 2023a.

Liu, Y. and Wang, T.: Worsening urban ozone pollution in China from 2013 to 2017 – Part 1: The complex and varying roles of meteorology, Atmos. Chem. Phys., 20, 6305–6321, https://doi.org/10.5194/acp-20-6305-2020, 2020.

Liu, Y., Geng, G., Cheng, J., Liu, Y., Xiao, Q., Liu, L., Shi, Q., Tong, D., He, K., and Zhang, Q.: Drivers of increasing ozone during the two phases of Clean Air Actions in China 2013–2020, Environ. Sci. Technol., 57, 8954–8964, https://doi.org/10.1021/acs.est.3c00054, 2023b.

Lu, X., Zhang, L., Chen, Y., Zhou, M., Zheng, B., Li, K., Liu, Y., Lin, J., Fu, T.-M., and Zhang, Q.: Exploring 2016–2017 surface ozone pollution over China: source contributions and meteorological influences, Atmos. Chem. Phys., 19, 8339–8361, https://doi.org/10.5194/acp-19-8339-2019, 2019.

Lundberg, S. M. and Lee, S.-I.: A unified approach to interpreting model predictions, Adv. Neural Inf. Process. Syst., 30, 4768–4777, https://doi.org/10.48550/arXiv.1705.07874, 2017.

Lundberg, S. M., Erion, G., Chen, H., DeGrave, A., Prutkin, J. M., Nair, B., Katz, R., Himmelfarb, J., Bansal, N., and Lee, S.-I.: From local explanations to global understanding with explainable AI for trees, Nat. Mach. Intell., 2, 56–67, https://doi.org/10.1038/s42256-019-0138-9, 2020.

Lyu, Y., Xu, H., Wu, H., Han, F., Lv, F., Kang, A., and Pang, X.: Spatiotemporal variations of $PM_{2.5}$ and ozone in urban agglomerations of China and meteorological drivers for ozone using explainable machine learning, Environ. Pollut., 365, 125380, https://doi.org/10.1016/j.envpol.2024.125380, 2025.

Mai, Z., Shen, H., Zhang, A., Sun, H. Z., Zheng, L., Guo, J., Liu, C., Chen, Y., Wang, C., Ye, J., Zhu, L., Fu, T.-M., Yang, X., and Tao, S.: Convolutional neural networks facilitate process understanding of megacity ozone temporal variability, Environ. Sci. Technol., 58, 15691–15701, https://doi.org/10.1021/acs.est.3c07907, 2024.

Mao, J., Tai, A. P. K., Yung, D. H. Y., Yuan, T., Chau, K. T., and Feng, Z.: Multidecadal ozone trends in China and implications for human health and crop yields: a hybrid approach combining a chemical transport model and machine learning, Atmos. Chem. Phys., 24, 345–366, https://doi.org/10.5194/acp-24-345-2024, 2024.

Meng, X., Jiang, J., Chen, T., Zhang, Z., Lu, B., Liu, C., Xue, L., Chen, J., Herrmann, H., and Li, X.: Chemical drivers of ozone change in extreme temperatures in eastern China, Sci. Total Environ., 874, 162424, https://doi.org/10.1016/j.scitotenv.2023.162424, 2023.

Ni, Y., Yang, Y., Wang, H., Wang, P., Li, K., Chen, L., Zhu, J., Li, B., and Liao, H.: Machine learning-based bias-corrected future projections of ozone concentrations from a chemistry-climate model, Environ. Sci. Technol., 60, 3135–3147, https://doi.org/10.1021/acs.est.5c11992, 2026.

Ren, H. H., Cheng, Y., Wu, F., Gu, Z. L., Cao, J. J., Huang, Y., Xue, Y. G., Cui, L., Zhang, Y. W., Chow, J. C., Watson, J. G., Zhang, R. J., Lee, S. C., Wang, Y. L., and Liu, S.: Spatiotemporal characteristics of ozone and the formation sensitivity over the Fenwei Plain, Sci. Total Environ., 881, 163369, https://doi.org/10.1016/j.scitotenv.2023.163369, 2023.

Ren, J., Guo, F., and Xie, S.: Diagnosing ozone–NO_x–VOC sensitivity and revealing causes of ozone increases in China based on 2013–2021 satellite retrievals, Atmos. Chem. Phys., 22, 15035–15047, https://doi.org/10.5194/acp-22-15035-2022, 2022.

Saeipourdizaj, P., Sarbakhsh, P., and Gholampour, A.: Application of imputation methods for missing values of PM_{10} and O_3 data: interpolation, moving average and K-nearest neighbor methods, Environ. Health Eng. Manag., 8, 215–226, https://doi.org/10.34172/EHEM.2021.25, 2021.

Tan, Y., Zhang, Y., Wang, T., Chen, T., Mu, J., and Xue, L.: Dissecting drivers of ozone pollution during the 2022 multicity lockdowns in China sheds light on future control direction, Environ. Sci. Technol., 58, 6988–6997, https://doi.org/10.1021/acs.est.4c01197, 2024.

Tong, L., Liu, Y., Meng, Y., Dai, X., Huang, L., Luo, W., Yang, M., Pan, Y., Zheng, J., and Xiao, H.: Surface ozone changes during the COVID-19 outbreak in China: an insight into the pollution characteristics and formation regimes of ozone in the cold season, J. Atmos. Chem., 80, 103–120, https://doi.org/10.1007/s10874-022-09443-2, 2023.

Vu, T. V., Shi, Z., Cheng, J., Zhang, Q., He, K., Wang, S., and Harrison, R. M.: Assessing the impact of clean air action on air quality trends in Beijing using a machine learning technique, Atmos. Chem. Phys., 19, 11303–11314, https://doi.org/10.5194/acp-19-11303-2019, 2019.

Wang, H., Liu, X., Wu, C., and Lin, G.: Regional to global distributions, trends, and drivers of biogenic volatile organic compound emission from 2001 to 2020, Atmos. Chem. Phys., 24, 3309–3328, https://doi.org/10.5194/acp-24-3309-2024, 2024.

Wang, L., Chen, B., Ouyang, J., Mu, Y., Zhen, L., Yang, L., Xu, W., and Tang, L.: Causal-inference machine learning reveals the drivers of China's 2022 ozone rebound, Environ. Sci. Ecotechnology, 24, 100524, https://doi.org/10.1016/j.ese.2025.100524, 2025a.

Wang, T., Xue, L., Brimblecombe, P., Lam, Y. F., Li, L., and Zhang, L.: Ozone pollution in China: a review of concentrations, meteorological influences, chemical precursors, and effects, Sci. Total Environ., 575, 1582–1596, https://doi.org/10.1016/j.scitotenv.2016.10.081, 2017.

Wang, T., Xue, L., Feng, Z., Dai, J., Zhang, Y., and Tan, Y.: Ground-level ozone pollution in China: a synthesis of recent findings on influencing factors and impacts, Environ. Res. Lett., 17, 063003, https://doi.org/10.1088/1748-9326/ac69fe, 2022a.

Wang, W., Parrish, D. D., Wang, S., Bao, F., Ni, R., Li, X., Yang, S., Wang, H., Cheng, Y., and Su, H.: Long-term trend of ozone pollution in China during 2014–2020: distinct seasonal and spatial

characteristics and ozone sensitivity, Atmos. Chem. Phys., 22, 8935–8949, https://doi.org/10.5194/acp-22-8935-2022, 2022b.

Wang, X., Zhu, J., Jiao, G., Chen, X., Yang, Z., Chen, L., Jin, X., and Liao, H.: Meteorological influence on surface ozone trends in China: assessing uncertainties caused by multi-dataset and multi-method, Atmos. Chem. Phys., 25, 13863–13878, https://doi.org/10.5194/acp-25-13863-2025, 2025b.

Wang, Y., Gong, C., Dong, L., and Huang, Y.: Estimation of near-surface high spatiotemporal resolution ozone concentration in China using Himawari-8 AOD, Remote Sens., 17, 528, https://doi.org/10.3390/rs17030528, 2025c.

Wang, Y., Wang, Y., Li, Q., Chen, T., Tan, Y., and Wang, T.: Synergy of natural sources exacerbates ozone pollution in China during drought–heatwave extremes, Environ. Sci. Technol., 59, 22739–22748, https://doi.org/10.1021/acs.est.5c07239, 2025.

Wei, J., Li, Z., Li, K., Dickerson, R. R., Pinker, R. T., Wang, J., Liu, X., Sun, L., Xue, W., and Cribb, M.: Full-coverage mapping and spatiotemporal variations of ground-level ozone (O_3) pollution from 2013 to 2020 across China, Remote Sens. Environ., 270, 112775, https://doi.org/10.1016/j.rse.2021.112775, 2022.

Weng, X., Forster, G. L., and Nowack, P.: A machine learning approach to quantify meteorological drivers of ozone pollution in China from 2015 to 2019, Atmos. Chem. Phys., 22, 8385–8402, https://doi.org/10.5194/acp-22-8385-2022, 2022.

Wu, K., Wang, Y., Qiao, Y., Liu, Y., Wang, S., Yang, X., Wang, H., Lu, Y., Zhang, X., and Lei, Y.: Drivers of 2013–2020 ozone trends in the Sichuan Basin, China: impacts of meteorology and precursor emission changes, Environ. Pollut., 300, 118914, https://doi.org/10.1016/j.envpol.2022.118914, 2022.

Xiang, Y., Zhang, T., Liu, J., Lv, L., Dong, Y., and Chen, Z.: Atmosphere boundary layer height and its effect on air pollutants in Beijing during winter heavy pollution, Atmos. Res., 215, 305–316, https://doi.org/10.1016/j.atmosres.2018.09.014, 2019.

Xue, J., Wang, F., Zhang, K., Zhai, H., Jin, D., Duan, Y., Yaluk, E., Wang, Y., Huang, L., Li, Y., Lei, T., Fu, Q., Fu, J. S., and Li, L.: Elucidate long-term changes of ozone in Shanghai based on an integrated machine learning method, Front. Environ. Sci. Eng., 17, 138, https://doi.org/10.1007/s11783-023-1738-5, 2023.

Yang, J. and Zhao, Y.: Performance and application of air quality models on ozone simulation in China – a review, Atmos. Environ., 293, 119446, https://doi.org/10.1016/j.atmosenv.2022.119446, 2023.

Yang, J., Wang, Y., Zhang, L., and Zhao, Y.: Investigating the response of China's surface ozone concentration to the future changes of multiple factors, Atmos. Chem. Phys., 25, 2649–2666, https://doi.org/10.5194/acp-25-2649-2025, 2025a.

Yang, L., Luo, H., Yuan, Z., Zheng, J., Huang, Z., Li, C., Lin, X., Louie, P. K. K., Chen, D., and Bian, Y.: Quantitative impacts of meteorology and precursor emission changes on the long-term trend of ambient ozone over the Pearl River Delta, China, and implications for ozone control strategy, Atmos. Chem. Phys., 19, 12901–12916, https://doi.org/10.5194/acp-19-12901-2019, 2019.

Yang, Y., Zhou, Y., Wang, H., Li, M., Li, H., Wang, P., Yue, X., Li, K., Zhu, J., and Liao, H.: Meteorological characteristics of extreme ozone pollution events in China and their future predictions, Atmos. Chem. Phys., 24, 1177–1191, https://doi.org/10.5194/acp-24-1177-2024, 2024.

Yang, Z., Li, Z., Cheng, F., Lv, Q., Li, K., Zhang, T., Zhou, Y., Zhao, B., Xue, W., and Wei, J.: Two-decade surface ozone (O_3) pollution in China: enhanced fine-scale estimations and environmental health implications, Remote Sens. Environ., 317, 114459, https://doi.org/10.1016/j.rse.2024.114459, 2025b.

Ye, X., Zhang, L., Wang, X., Lu, N., Hickman, S., Luo, G., and Archibald, A. T.: Deciphering the impacts of meteorology on surface ozone variability in eastern China using explainable machine learning models, Atmos. Chem. Phys., 26, 6377–6390, https://doi.org/10.5194/acp-26-6377-2026, 2026.

Zhang, L., Wang, L., Ji, D., Xia, Z., Nan, P., Zhang, J., Li, K., Qi, B., Du, R., Sun, Y., Wang, Y., and Hu, B.: Explainable ensemble machine learning revealing the effect of meteorology and sources on ozone formation in megacity Hangzhou, China, Sci. Total Environ., 922, 171295, https://doi.org/10.1016/j.scitotenv.2024.171295, 2024.

Zhang, X., Zhang, W.-C., Wu, W., and Liu, H.-B.: Understanding ozone variability in spatial responses to emissions and meteorology in China using interpretable machine learning, iScience, 28, 113036, https://doi.org/10.1016/j.isci.2025.113036, 2025.

Zhou, W., Lei, L., Du, A., Zhang, Z., Li, Y., Yang, Y., Tang, G., Chen, C., Xu, W., Sun, J., Li, Z., Fu, P., Wang, Z., and Sun, Y.: Unexpected increases of severe haze pollution during the post COVID-19 period: effects of emissions, meteorology, and secondary production, J. Geophys. Res.-Atmos., 127, e2021JD035710, https://doi.org/10.1029/2021JD035710, 2022.